Geophysical Research Letters

RESEARCH LETTER
10.1029/2025GL115024

Ab Initio Study of the Conductivities of B2 FeSi Under Core-Mantle Boundary Conditions

Yonghui Huang[1,2], Yunguo Li[1,2], Dario Alfè[3,4], Monica Pozzo[3,5,6], and Huaiwei Ni[1,2]

[1]State Key Laboratory of Lithospheric and Environmental Coevolution, University of Science and Technology of China, Hefei, China, [2]Deep Space Exploration Laboratory/School of Earth and Space Sciences, USTC, Hefei, China, [3]Department of Earth Sciences, University College London, London, UK, [4]Università di Napoli Federico II, Dipartimento di Fisica "Ettore Pancini", Napoli, Italy, [5]Faculty of Technological & Innovation Sciences, Universitas Mercatorum, Roma, Italy, [6]Institute for Materials Discovery, UCL East, London, UK

Key Points:

- B2 FeSi has a thermal conductivity of 109 W m^{-1} K^{-1}, about 11 times of those of mantle minerals
- The presence of B2 FeSi in the ultra-low velocity zones (ULVZs) would create heat anomalies with increased heat flux
- These ULVZs could serve as cooling spots, driving convection in the outer core and contributing to the Earth's dynamo

Supporting Information:

Supporting Information may be found in the online version of this article.

Correspondence to:

Y. Li,
liyunguo@ustc.edu.cn

Citation:

Huang, Y., Li, Y., Alfè, D., Pozzo, M., & Ni, H. (2025). Ab initio study of the conductivities of B2 FeSi under core-mantle boundary conditions. *Geophysical Research Letters*, *52*, e2025GL115024. https://doi.org/10.1029/2025GL115024

Received 4 FEB 2025
Accepted 2 MAY 2025

Author Contributions:

Conceptualization: Yunguo Li
Data curation: Yonghui Huang
Formal analysis: Yonghui Huang, Yunguo Li, Dario Alfè, Monica Pozzo, Huaiwei Ni
Funding acquisition: Yunguo Li
Investigation: Yonghui Huang
Methodology: Yonghui Huang, Yunguo Li
Project administration: Yunguo Li
Supervision: Yunguo Li
Validation: Dario Alfè
Visualization: Yonghui Huang
Writing – original draft: Yonghui Huang, Yunguo Li
Writing – review & editing: Yunguo Li, Dario Alfè, Monica Pozzo, Huaiwei Ni

Abstract While the ultra-low velocity zones (ULVZs) may hold key information about deep Earth dynamics, their elusive state and origin remain enigmatic. Recent high-pressure experiments suggest that ULVZs may originate from the B2 FeSi crystallization from the outer core. Understanding the conductivity of the B2 phase can shed light on its role in deep mantle dynamics and serve as a test for its presence at the core-mantle boundary (CMB). Here, we calculated the thermal and electrical conductivities of B2 $Fe_{1-x}Si_x$ at 127 GPa and up to 4,500 K using first-principles molecular dynamics. Our results show that under CMB conditions, the thermal and electrical conductivities of B2 FeSi are significantly higher than those of lower-mantle minerals. The exceptionally high conductivities of B2 FeSi would enhance heat transfer and elevate temperatures within ULVZs, if B2 FeSi is present, thereby promoting the core dynamo and powering hotspots, consistent with seismic observations of ULVZs.

Plain Language Summary The ultra-low velocity zones (ULVZs) are anomalies at the core-mantle boundary (CMB), identified by their extremely low seismic velocities. However, their origins and conductive properties remain uncertain. Recent high-pressure experiments suggest that ULVZs may form from the B2 FeSi phase, crystallized from the outer core containing hydrogen and silicon. To better understand the conductive properties of B2 FeSi and its impact, we used first-principles calculations to determine its thermal and electrical conductivities under CMB conditions. Our results show that B2 FeSi has the highest thermal conductivity compared to mantle minerals. This makes ULVZs heat anomalies characterized by high thermal conductivity, high temperature, and high heat flux. Consequently, ULVZs could act as cooling spots at the top of the outer core, driving convection in the outer core and helping maintain the Earth's dynamo and geomagnetic field.

1. Introduction

Ultra-low velocity zones (ULVZs) are distinguished by their exceptionally low shear and compressional wave velocities compared to the surrounding mantle rocks (Brown et al., 2015; Idehara, 2011). These smaller-scale ULVZs are scattered throughout the D″ layer, particularly around the Large Low Shear Velocity Provinces, and are found near subduction zones, intraplate hotspots, and other geological features (Yu & Garnero, 2018). Typically ranging from tens to a few dozen kilometers in size, ULVZs are potentially widespread throughout the D″ layer but are difficult to detect precisely due to their thinness (Cottaar & Romanowicz, 2012). The origin of ULVZs is perplexing, but could offer valuable insights into the evolution of the lower mantle.

The densities of ULVZs are higher than their surroundings, leading to hypotheses that they are enriched in iron, partially molten, or a combination of both. Various scenarios have been proposed for the iron enrichment: entrainment of iron from the core, accumulation from past subduction events (Dobson & Brodholt, 2005; Hirose et al., 2005), remnants of a basal magma ocean (Pachhai et al., 2022), Fe-bearing materials from the interactions with the outer core (Knittle & Jeanloz, 1991; J. Liu et al., 2017; Mao et al., 2006; Mergner et al., 2021; Wicks et al., 2017). On the other hand, temperature may play an important role in the formation of ULVZs. Many studies indicate that ULVZs are correlated with partial melting, likely due to higher temperature (Berryman, 2000; Garnero & Vidale, 1999; Havens & Revenaugh, 2001; Reasoner & Revenaugh, 2000; Rost et al., 2006; Williams & Garnero, 1996). In addition, the association of ULVZs' locations with hotspots feeding mantle plumes also implies high temperature of ULVZs (Cottaar & Romanowicz, 2012; Garnero, 2000; Williams et al., 1998), but the origin of temperature anomaly is also mysterious.

Recently, high-pressure experiments (Fu et al., 2023) proposed an alternative origin for ULVZs based on interactions involving an Fe-Si-H outer core melt—a composition whose plausibility is supported by subsequent studies identifying hydrogen and silicon as preferred light elements in the core (T. Liu & Jing, 2024a). Fu et al. (2023) found that B2 FeSi crystallized from such melts in the presence of hydrogen within the outer core's temperature-pressure conditions near the core-mantle boundary (CMB). The low density of B2 FeSi relative to the surrounding liquid causes it to rise buoyantly toward the CMB. Furthermore, the study reveals that B2 FeSi crystallized from Fe-Si-H melts in the outer core exhibits an almost perfect 1:1 ratio of iron to silicon. This remarkable stoichiometry distinguishes it from previously studied Fe-Si alloys. Presence of B2 FeSi can explain the seismic characters of ULVZs, and the content of FeSi in ULVZs could be as high as 27–39 vol% (T. Liu & Jing, 2024b).

The conductivity of B2 FeSi under CMB conditions is then becoming crucial for understanding the origin of temperature anomalies of ULVZs: can B2 FeSi heat up ULVZs and induce higher temperatures, or must other mechanism be invoked? Additionally, the thermal and electrical conductivities of B2 FeSi are important for evaluating the impact of FeSi on heat transfer, the geodynamo, and mantle dynamics. These properties also serve as a test for the existence of B2 FeSi in ULVZs. Previous studies indicate that Si incorporation into Fe significantly reduces thermal conductivity under core conditions (De Koker et al., 2012), challenging the possible existence of the B2 phase in ULVZs. Besides, studies at lower temperatures suggest that B2 FeSi behaves as a semiconductor (Zhao et al., 2011), which imply low conductivities of B2 FeSi. But it may undergo a band gap narrowing or even transition to a conductive state at high pressure and high temperature.

In this work, we employed Ab initio molecular dynamics (AIMD) and the Kubo-Greenwood equation to calculate electrical and thermal conductivities of B2 FeSi under different stoichiometries and temperatures at 127 GPa. We then compared the thermal conductivities of B2 FeSi with mantle and core materials, and investigated their impact on heat transfer and heat structure at CMB.

2. Methods

Ab initio calculations of transport properties based on density functional theory have been widely used in the past decades due to their high accuracy comparable with experiments, and lack of limitations on pressure and temperature. Following previous studies, we used AIMD and the Kubo-Greenwood formula to calculate conductivities. AIMD was performed using the VASP code (Blöchl, 1994; Kresse & Joubert, 1999). Based on previous studies and our tests, we considered system sizes of 128 atoms for the B2 phase $Fe_{1-x}Si_x$. The exchange-correlation potential is represented in the generalized gradient approximation (GGA-PBE) (Perdew et al., 1996), with valence electrons represented as planewaves with a cutoff of 600 eV (this converges the transport properties to an accuracy of 0.01%) in the projector augmented wave formalism (Kresse & Furthmüller, 1996; Kresse & Hafner, 1993). We used valence electron configuration $3d^74s^1$ for Fe and $3s^23p^2$ for Si. The 8-electron pseudopotential of Fe produces results closer to experiments (Sun et al., 2018) and there is basically no difference between the electronic states around Fermi level calculated by different pseudopotentials (see Figure S1 in Supporting Information S1). In our study, only the most iron-rich Fe_5Si_3 is magnetic. But, there is basically no difference between the spinpolarized and non-spinpolarized calculations for thermal conductivity (Figure S2 in Supporting Information S1). Simulations were performed in the NVT ensemble with average pressure of 127 GPa, and temperatures of 3,500, 4,000, and 4,500 K, and run over at least 7 ps of simulation time after equilibration. The time dependent mean square displacement was used to check that systems are indeed in the solid state.

From each AIMD trajectory, we extracted atomic configuration snapshots every 500 fs from the last 5 ps to compute the electrical and thermal conductivity. The velocity autocorrelation functions for our simulations decay within 200 fs, indicating that a 500 fs time separation is sufficient for individual snapshots to be uncorrelated. This approach provides a representative sampling of the solid structure at each composition-temperature point. We tested the number of k points from 8, 16, 32, and 64–96, and found the conductivities will converge when the number of k points reaches 64 (see Figure S3 in Supporting Information S1). For each snapshot from the AIMD, we chose 12 specific k points from the 96 k points to reduce the amount of calculations, and make sure the difference is within 3% (the values from the special 12 k points and their average are the closest to the average value from the 96 k points).

We consider only the electronic contribution to represent the total thermal conductivity. Previous studies have shown that, under core conditions, the ionic contribution to the thermal conductivity of iron is merely 2.5–4 W m^{-1} K^{-1}, accounting for only about 1%–2% of the electronic contribution (Pozzo et al., 2012). Electronic transport properties σ_{el} and k_{el} were computed using the Kubo-Greenwood equation, as implemented in the KG4VASP code (Di Paola et al., 2020). σ_{el} and k_{el} are expressed as

$$\sigma_{el} = L_{11} \tag{1}$$

$$k_{el} = \frac{1}{e^2 T}\left(L_{22} - \frac{L_{12}^2}{L_{11}}\right) \tag{2}$$

where L_{ij} are the Onsager coefficients (i,j = 1 or 2), which are

$$L_{ij} = (-1)^{(i+j)}\frac{he^2}{V_{cell}}\sum_{k',k}\lim_{\epsilon\to 0}\frac{f(\epsilon_{k'}) - f(\epsilon_k)}{\epsilon}\delta(\epsilon_{k'} - \epsilon_k - \epsilon) \times \langle\psi_k|\hat{v}|\psi_{k'}\rangle\langle\psi_{k'}|\hat{v}|\psi_k\rangle(\epsilon_{k'} - \epsilon_F)^{i-1}(\epsilon_k - \epsilon_F)^{j-1} \tag{3}$$

where ϵ_F is the Fermi energy; ψ_k, ϵ_k, and $f(\epsilon_k)$ are the wave function, eigenvalue, and Fermi-Dirac occupation of eigenstate k, respectively; $\hat{v}$ is the velocity operator; and V_{cell} is the simulation cell volume. For a given snapshot, the self-consistent electronic relaxation was performed with electronic states populated according to the Mermin functional (Mermin, 1965). ψ_k and ϵ_k are represented by the Kohn-Sham eigenfunctions and eigenvalues for each given snapshot, while $\hat{v}$ is computed from the Hamiltonian gradient, $h\hat{v} = 2\pi\partial\hat{H}/\partial k$. Regarding the electron-electron scattering not fully accounted for in the Kubo-Greenwood approach, previous studies on the thermal conductivity of Fe and Fe-Si alloys (Zhang et al., 2020, 2022) have shown that electron-electron scattering can contribute to an increase of up to 10% in the thermal conductivity of pure hcp Fe, but this contribution decreases rapidly with increasing Si content. In our study, the lowest Si content is approximately 40 wt%, a level at which electron-electron scattering can be reasonably neglected.

The Wiedemann-Franz law states that the ratio of the electronic contribution of the thermal conductivity to the electrical conductivity of a metal is proportional to the temperature (T),

$$\frac{k_{el}}{\sigma_{el}} = LT \tag{4}$$

where L, known as the Lorenz number, is theoretically equal to 2.44×10^{-8} W Ω K^{-2}.

To simulate the heat flux and temperature gradient at the CMB, we need to use the heat equations,

$$\frac{\partial u}{\partial t} = \frac{\kappa}{c_p\rho}\nabla^2 u = \frac{\kappa}{c_p\rho}\left(\frac{\partial^2 u}{\partial x^2} + \frac{\partial^2 u}{\partial y^2} + \frac{\partial^2 u}{\partial z^2}\right) \tag{5}$$

$$q = -\kappa\nabla u \tag{6}$$

where $u = u(x,y,z,t)$ is the temperature as a function of space and time, κ is the thermal conductivity, c_p is the specific heat capacity, ρ is the mass density, and $q = q(x,y,z,t)$ is a vector field that represents the magnitude and direction of the heat flow. Equations 5 and 6 describe how heat diffuses through a given region. By giving proper boundary conditions, we can use finite element method to solve the problem.

3. Results and Discussion

3.1. Calculated Thermal and Electrical Conductivities

We calculated the thermal and electrical conductivities of B2 FeSi at CMB conditions. Besides, to elucidate the compositional effects and facilitate a comparison with previous studies, we also considered two non-stoichiometric compositions of B2 structure: Fe_5Si_3 enriched in Fe and Fe_3Si_5 enriched in Si. The symmetrical crystal structures for the nonstoichiometric compositions were used. The calculated conductivities and Lorenz number are shown in Figure 1.

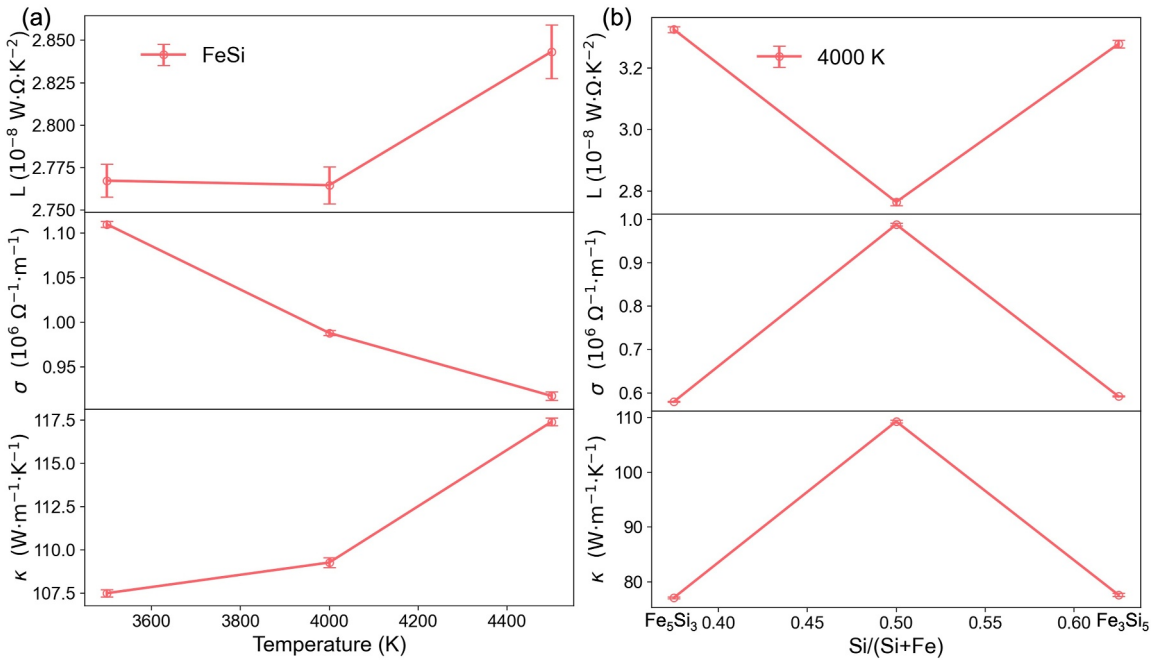

Figure 1. Electrical and thermal conductivities of the B2 FeSi phase and the corresponding Lorenz number with (a) different temperatures and (b) compositions.

As shown in Figure 1b, our results at 4,000 K indicate that the electrical and thermal conductivities of the Fe-rich and Si-rich compositions are similar. In contrast, the FeSi composition, adhering to the stoichiometric ratio, significantly outperforms the other two. In addition, a composition-based symmetry is observed in Figure 1b, which has also been observed in previous studies on B2-type aluminides (Terada et al., 2002). Specifically, the electrical conductivity of FeSi reaches approximately $0.99 \times 10^6\ \Omega^{-1}\ m^{-1}$, nearly twice that of the other compositions. The thermal conductivity of FeSi is approximately 109 W m^{-1} K^{-1}, 50% higher than the other two.

To further explore these properties, we invoke the Wiedemann-Franz law, which posits that the ratio of thermal conductivity to electrical conductivity in metals is directly proportional to temperature. This ratio, known as the Lorenz number, theoretically equals $2.44 \times 10^{-8}\ W\ \Omega\ K^{-2}$. However, deviations from this ideal value occur due to varying interactions within different materials. Our computed Lorenz numbers of 3.33×10^{-8}, 2.77×10^{-8}, and $3.28 \times 10^{-8}\ W\ \Omega\ K^{-2}$ for all three compositions at 4,000 K exhibit a little bit deviation from the theoretical value.

As shown in Figure 1a, the thermal conductivity of B2 FeSi experiences a modest increase with rising temperature. It increases from approximately 108 W m^{-1} K^{-1} at 3,500 K to 117 W m^{-1} K^{-1} at 4,500 K. Remarkably, B2 FeSi maintains high thermal conductivity across a substantial temperature range. By contrast, the electrical conductivity of B2 FeSi exhibits a moderate decline as temperature increases. It decreases from approximately $1.1 \times 10^6\ \Omega^{-1}\ m^{-1}$ at 3,500 K to $0.92 \times 10^6\ \Omega^{-1}\ m^{-1}$ at 4,500 K. Consequently, the Lorenz number experiences a slight increase from 3,500 to 4,500 K. The contrasting temperature dependencies of thermal and electrical conductivities likely arise from distinct conduction mechanisms. As temperature increases, electron excitation intensifies, but the mean free path for both electrons and phonons decrease due to increased scattering. This decrease in mean free path significantly reduces electrical conductivity, while it has a smaller impact on thermal conductivity because phonon-mediated heat transfer can still be efficient. Consequently, the thermal and electrical conductivities exhibit different dependencies on temperature.

As a comparative validation, we also computed the thermal conductivity of hcp Fe at 4,000 K and ∼127 GPa, yielding approximately 140 W m^{-1} K^{-1}, a value consistent with literature references (Kleinschmidt et al., 2023). These results collectively reinforce the validity of our findings.

To further analyze the anomalous high conductivity of B2 FeSi, we computed the density of states (DOS) of B2 FeSi, Fe_3Si_5, Fe_5Si_3, and hcp Fe at different temperatures. As previously mentioned, B2 FeSi exhibits a semiconducting behavior at low pressures and temperatures, characterized by a band gap in the DOS near the highest

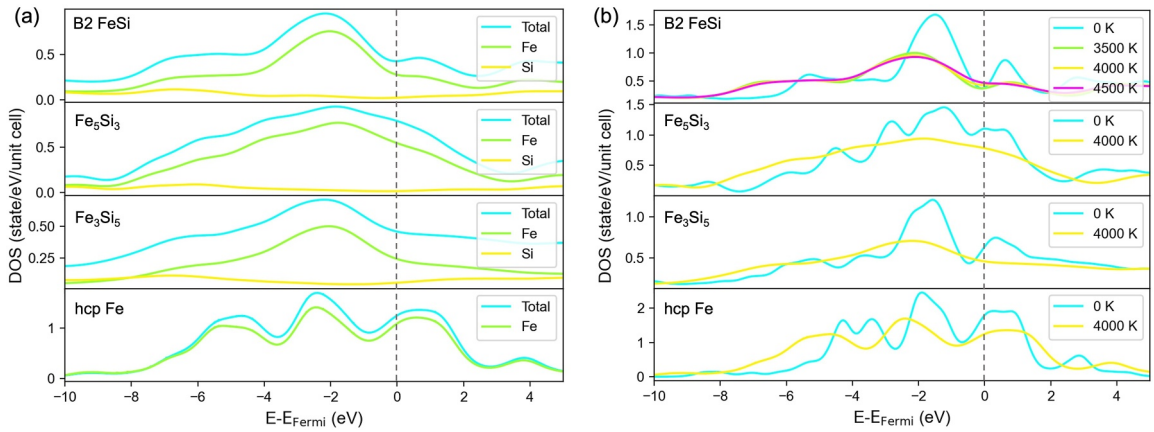

Figure 2. The density of states (DOS) of B2 FeSi, Fe_3Si_5, Fe_5Si_3, and hcp Fe. (a) The total and partial DOSs at 4,000 K and (b) the total DOS at different temperatures.

occupied state (Fermi level). This gap prevents electrons from freely transitioning to unoccupied states above the Fermi level, thereby impeding electrical and thermal conduction. However, B2 FeSi at CMB conditions has a closed bandgap and displays metallic properties as shown in Figure 2, indicating a semiconducting-to-metallic transition under pressures.

Figure 2a illustrates the DOS for the four materials, including the individual DOS for Fe and Si as well as the total DOS. We have shifted the DOS to align the Fermi level with the energy zero point. The DOS of hcp Fe significantly differs from those of the other three materials. Fe predominantly shapes the DOS in the B2 FeSi, Fe_3Si_5, and Fe_5Si_3, and Si contributes minimally to the total DOS. However, the Si content significantly impacts the DOS shape. Comparing B2 FeSi, Fe_3Si_5, and Fe_5Si_3, Fe_3Si_5 exhibits a DOS shape similar to B2 FeSi, with a narrow peak below the Fermi level. By contrast, Fe_5Si_3 displays a flatter DOS profile. Among the three, B2 FeSi's total DOS exhibits the sharpest peak just below the Fermi level, indicating a higher concentration of states immediately adjacent to the Fermi level and thus enhanced conduction properties. We also compare the DOS of B2 FeSi at three temperatures: 3,500, 4,000, and 4,500 K (Figure 2b). Although subtle, the DOS shift slightly toward higher energies with increasing temperature. At 4,500 K, more states aggregate just below the Fermi level, contributing to improved thermal conductivity. In summary, the DOS analysis sheds light on the underlying mechanisms driving B2 FeSi's exceptional conductivity. Its unique DOS distribution near the Fermi level, combined with temperature effects, contributes to its enhanced thermal and electrical properties.

3.2. Implications to the Deep Earth

Having established the exceptional conductivity of B2 FeSi, we now seek to understand its implications within the deep Earth. To this end, we have compiled thermal conductivity data from both experiments and theoretical calculations, covering various compositional scenarios. Figure 3 includes those relevant to the lower mantle (such as $MgSiO_3$ perovskite and post-perovskite, as well as MgO with and without Fe), and also compositions relevant to core ranging from pure Fe to Fe-Si, Fe-O, and Fe-Si-O alloys and liquids.

As shown in Figure 3, most studies consistently observe a gradual increase of thermal conductivity with rising temperature—a trend that aligns with our calculation results for B2 FeSi. At 4,000 K, the thermal conductivities of various Fe alloys and liquids (including Fe-Si-O) cluster around 100 W m^{-1} K^{-1}. Notably, our calculated values for B2 FeSi closely match literature data. The Fe-Si-O melts and liquid Fe, representing conditions near the CMB, exhibit slightly higher thermal conductivities in the range of 140–160 W m^{-1} K^{-1}. Most mantle minerals fall within the 5–20 W m^{-1} K^{-1} range, with the exception of MgO, which boasts an exceptionally high thermal conductivity of 76.8 W m^{-1} K^{-1}. In summary, our study indicates that under the CMB conditions, B2 FeSi not only surpasses other mantle minerals in thermal conductivity but even approaches that of liquid outer core. Consequently, B2 FeSi-containing ULVZs could emerge as potential contributors to thermal anomalies at the CMB.

Previous studies suggest that blending approximately 8 vol% of B2 FeSi can account for the reduced seismic wave velocities observed in ULVZs relative to the surrounding mantle (Mergner et al., 2021), but also a more recent

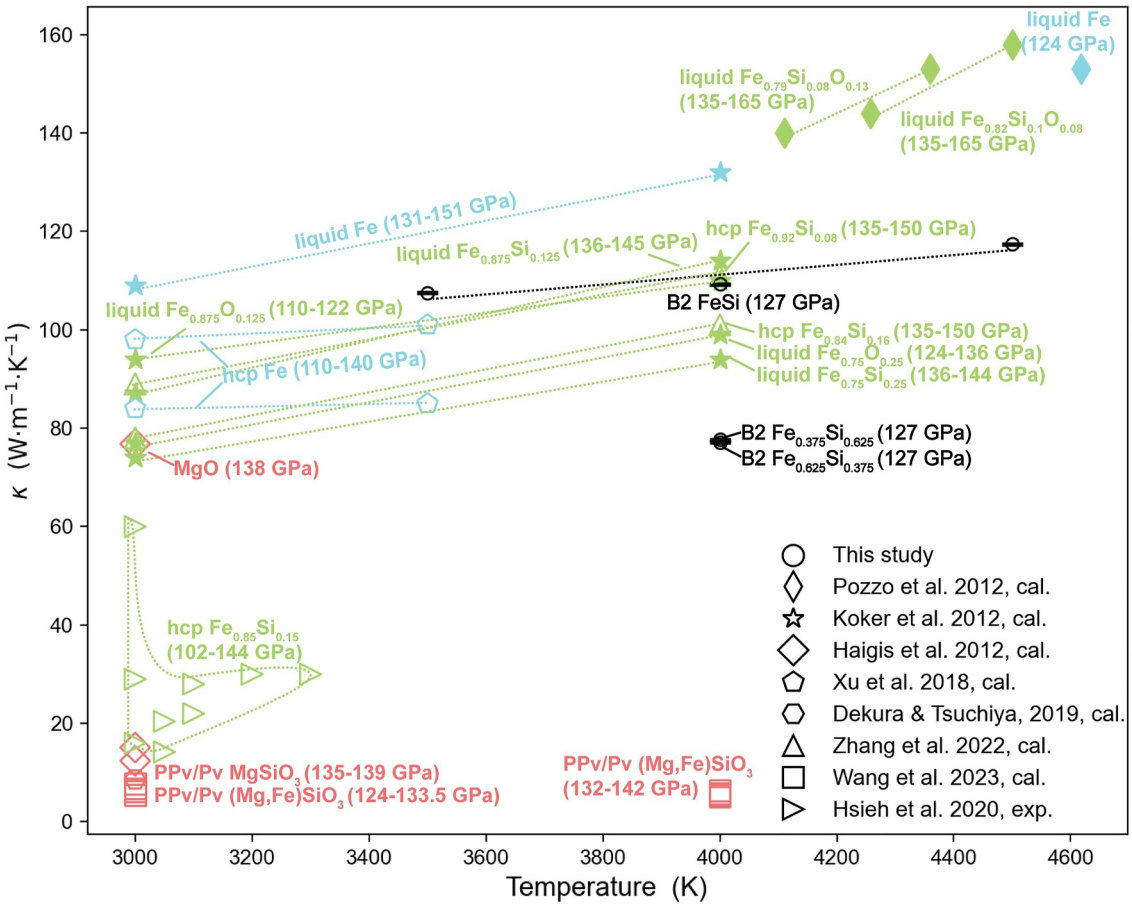

Figure 3. Comparison of the calculated thermal conductivity of B2 FeSi with literature data (De Koker et al., 2012; Dekura & Tsuchiya, 2019; Haigis et al., 2012; Hsieh et al., 2020; Pozzo et al., 2012; Wang et al., 2023; Xu et al., 2018; Zhang et al., 2022). Different marker shapes represent various studies, while colors denote distinct materials. Solid and hollow markers differentiate between different states.

study suggests a much higher ratio of 27–39 vol% B2 FeSi (T. Liu & Jing, 2024b). Furthermore, the addition of high-conductivity B2 FeSi would correspondingly elevate the thermal conductivity of ULVZs. The thermal conductivity of mixtures involving B2 FeSi and mantle minerals can be calculated by using the Hashin-Shtrikman theory, from which the upper and lower bounds of the mixture's thermal conductivity are as follows

$$\kappa_{\text{lower}} = \kappa_1 + \frac{f_2}{(\kappa_2 - \kappa_1)^{-1} + f_1(3\kappa_1)^{-1}} \tag{7}$$

$$\kappa_{\text{upper}} = \kappa_2 + \frac{f_1}{(\kappa_1 - \kappa_2)^{-1} + f_2(3\kappa_2)^{-1}} \tag{8}$$

Here κ_{upper} and κ_{lower} represent the upper and lower limits of the mixture's thermal conductivity, respectively. The composition-dependent factors f_1 and f_2 denote the volume fractions of the initial components. κ_1 and κ_2 correspond to the thermal conductivities of the two initial constituents. Our calculations, assuming a mantle mineral thermal conductivity of 10 W m^{-1} K^{-1} and B2 FeSi's thermal conductivity of 109 W m^{-1} K^{-1}, yield a thermal conductivity of 12–16 W m^{-1} K^{-1} when B2 FeSi constitutes 8 vol% of the mixture. And if we use the latest results of 27–39 vol% B2 FeSi, the thermal conductivity of the ULVZs could reach to about 18–41 W m^{-1} K^{-1}.

We built a simple model of heat transport to quantify the influence of the B2 FeSi in the ULVZs. Based on the heat equation and boundary conditions. Assuming the temperature anomaly caused by the ULVZs is limited in the D″ layer, then the lower and upper boundaries of the temperature anomaly area are about 2,900 and 2,700 km. The boundary temperatures are fixed values and are set to 3,500 and 2,500 K, respectively. Then we set the thermal

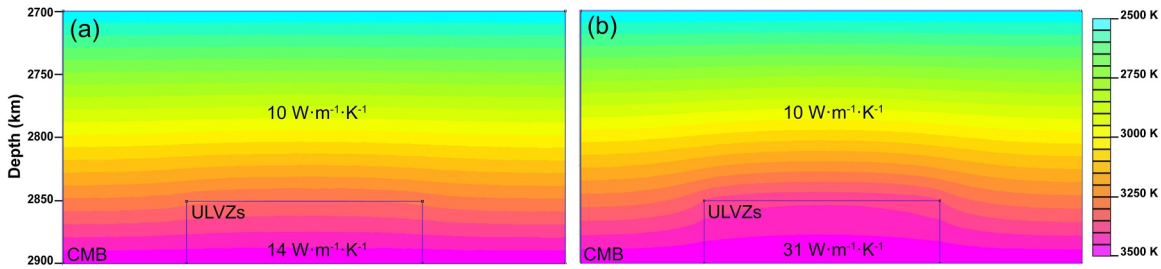

Figure 4. Simulated temperature profile at core-mantle boundary with ultra-low velocity zones (ULVZs). The thermal conductivity of ULVZs was set as (a) 14 and (b) 31 W m^{-1} K^{-1}, representing ULVZs with 8 vol% and 39% B2 FeSi, respectively.

conductivity of the mantle to 10 W m^{-1} K^{-1}, and that of ULVZs to 14 and 31 W m^{-1} K^{-1}, respectively, representing the midpoints between the upper and lower bounds of the mixture as predicted by the Hashin-Shtrikman theory. The thickness of ULVZs is 50 km. We use the Finite Element Method Magnetics (Meeker, 2010) code to solve the heat flow problem, and the results are shown in Figure 4. The thermal anomaly at the top of ULVZs is about 50–100 K higher. The heat flux through ULVZs is about 1.2–1.8 times higher than the mantle. Thus, the presence of B2 FeSi supports the formation of heat anomalies in ULVZs. The absence of heat anomalies only occurs when we used the lowest fraction of B2 FeSi and the highest reported thermal conductivity of mantle minerals (see Figure S4 in Supporting Information S1).

In the core dynamics, buoyancy drives convection due to density variations as a result of compositional and temperature differences. On one hand, the precipitation of relatively lighter B2 FeSi increases the melt's density, promoting subsidence and convection. On the other hand, the high thermal conductivity of ULVZs enhances heat flux, facilitating heat dissipation and convection within the outer core. At the same time, this increased heat flux may impact estimates of heat flow across the CMB. Although currently detected ULVZs constitute only a small portion of the D″ layer, they could significantly influence heat flow across the CMB if widespread thin layers of ULVZs exist within the D″ layer.

4. Conclusions

We calculated the thermal and electrical conductivities of both stoichiometric and nonstoichiometric B2 FeSi under CMB conditions using ab initio methods. Unlike its semiconducting behavior at low pressures, B2 FeSi becomes metallic and exhibits high thermal and electrical conductivities under CMB conditions. The thermal conductivity of stoichiometric B2 FeSi is about 80% of outer core components and 11 times of those of lower-mantle minerals. The presence of B2 FeSi in ULVZs can create heat anomalies at the CMB, drive core convection, and power mantle plumes. This supports the proposal that B2 FeSi constitutes ULVZs, which could be further verified by using our calculated electrical conductivities in future electromagnetic induction studies.

Data Availability Statement

Ab initio molecular dynamics data are deposited in the repository Mendeley Data (Huang, 2025).

Acknowledgments
The authors acknowledge the support of National Natural Science Foundation of China (42322201 and 42173040). Y.L. also thanks the support from CAS Hundred Talents Program. D.A. and M.P. acknowledge support from the Natural Environment Research Council (NERC) grant numbers 331 NE/M000990/1 and NE/R000425/1. The numerical calculations in this paper have been done on the supercomputing system in the Supercomputing Center of University of Science and Technology of China and in the Hefei Advanced Computing Center. This work also used the ARCHER2 UK National SupercomputingService (https://www.archer2.ac.UK).

References

Berryman, J. G. (2000). Seismic velocity decrement ratios for regions of partial melt in the lower mantle. *Geophysical Research Letters*, *27*(3), 421–424. https://doi.org/10.1029/1999gl008402

Blöchl, P. E. (1994). Projector augmented-wave method. *Physical Review B*, *50*(24), 17953–17979. https://doi.org/10.1103/physrevb.50.17953

Brown, S. P., Thorne, M. S., Miyagi, L., & Rost, S. (2015). A compositional origin to ultralow-velocity zones. *Geophysical Research Letters*, *42*(4), 1039–1045. https://doi.org/10.1002/2014gl062097

Cottaar, S., & Romanowicz, B. (2012). An unsually large ULVZ at the base of the mantle near Hawaii. *Earth and Planetary Science Letters*, *355*, 213–222. https://doi.org/10.1016/j.epsl.2012.09.005

De Koker, N., Steinle-Neumann, G., & Vlček, V. (2012). Electrical resistivity and thermal conductivity of liquid Fe alloys at high P and T, and heat flux in Earth's core. *Proceedings of the National Academy of Sciences of the United States of America*, *109*(11), 4070–4073. https://doi.org/10.1073/pnas.1111841109

Dekura, H., & Tsuchiya, T. (2019). Lattice thermal conductivity of $MgSiO_3$ postperovskite under the lowermost mantle conditions from ab initio anharmonic lattice dynamics. *Geophysical Research Letters*, *46*(22), 12919–12926. https://doi.org/10.1029/2019gl085273

Di Paola, C., Macheda, F., Laricchia, S., Weber, C., & Bonini, N. (2020). First-principles study of electronic transport and structural properties of $Cu_{12}Sb_4S_{13}$ in its high-temperature phase. *Physical Review Research*, *2*(3), 033055. https://doi.org/10.1103/PhysRevResearch.2.033055

Dobson, D. P., & Brodholt, J. P. (2005). Subducted banded iron formations as a source of ultralow-velocity zones at the core–mantle boundary. *Nature*, *434*(7031), 371–374. https://doi.org/10.1038/nature03430

Fu, S., Chariton, S., Prakapenka, V. B., & Shim, S.-H. (2023). Core origin of seismic velocity anomalies at Earth's core–mantle boundary. *Nature*, *615*(7953), 646–651. https://doi.org/10.1038/s41586-023-05713-5

Garnero, E. J. (2000). Heterogeneity of the lowermost mantle. *Annual Review of Earth and Planetary Sciences*, *28*(1), 509–537. https://doi.org/10.1146/annurev.earth.28.1.509

Garnero, E. J., & Vidale, J. E. (1999). ScP; a probe of ultralow velocity zones at the base of the mantle. *Geophysical Research Letters*, *26*(3), 377–380. https://doi.org/10.1029/1998gl900319

Haigis, V., Salanne, M., & Jahn, S. (2012). Thermal conductivity of MgO, $MgSiO_3$ perovskite and post-perovskite in the Earth's deep mantle. *Earth and Planetary Science Letters*, *355–356*, 102–108. https://doi.org/10.1016/j.epsl.2012.09.002

Havens, E., & Revenaugh, J. (2001). A broadband seismic study of the lowermost mantle beneath Mexico: Constraints on ultralow velocity zone elasticity and density. *Journal of Geophysical Research*, *106*(B12), 30809–30820. https://doi.org/10.1029/2000jb000072

Hirose, K., Takafuji, N., Sata, N., & Ohishi, Y. (2005). Phase transition and density of subducted MORB crust in the lower mantle. *Earth and Planetary Science Letters*, *237*(1–2), 239–251. https://doi.org/10.1016/j.epsl.2005.06.035

Hsieh, W. P., Goncharov, A. F., Labrosse, S., Holtgrewe, N., Lobanov, S. S., Chuvashova, I., et al. (2020). Low thermal conductivity of iron-silicon alloys at Earth's core conditions with implications for the geodynamo. *Nature Communications*, *11*(1), 3332. https://doi.org/10.1038/s41467-020-17106-7

Huang, Y. (2025). Ab initio study of the conductivities of B2 FeSi under core-mantle boundary conditions. *Mendeley Data*, *V1*. https://doi.org/10.5194/egusphere-egu24-13850

Idehara, K. (2011). Structural heterogeneity of an ultra-low-velocity zone beneath the Philippine Islands: Implications for core–mantle chemical interactions induced by massive partial melting at the bottom of the mantle. *Physics of the Earth and Planetary Interiors*, *184*(1–2), 80–90. https://doi.org/10.1016/j.pepi.2010.10.014

Kleinschmidt, U., French, M., Steinle-Neumann, G., & Redmer, R. (2023). Electrical and thermal conductivity of fcc and hcp iron under conditions of the Earth's core from ab initio simulations. *Physical Review B*, *107*(8), 085145. https://doi.org/10.1103/physrevb.107.085145

Knittle, E., & Jeanloz, R. (1991). Earth's core-mantle boundary: Results of experiments at high pressures and temperatures. *Science*, *251*(5000), 1438–1443. https://doi.org/10.1126/science.251.5000.1438

Kresse, G., & Furthmüller, J. (1996). Efficiency of ab-initio total energy calculations for metals and semiconductors using a plane-wave basis set. *Computational Materials Science*, *6*(1), 15–50. https://doi.org/10.1016/0927-0256(96)00008-0

Kresse, G., & Hafner, J. (1993). Ab initio molecular dynamics for open-shell transition metals. *Physical Review B*, *48*(17), 13115–13118. https://doi.org/10.1103/physrevb.48.13115

Kresse, G., & Joubert, D. (1999). From ultrasoft pseudopotentials to the projector augmented-wave method. *Physical Review B*, *59*(3), 1758–1775. https://doi.org/10.1103/physrevb.59.1758

Liu, J., Hu, Q., Young Kim, D., Wu, Z., Wang, W., Xiao, Y., et al. (2017). Hydrogen-bearing iron peroxide and the origin of ultralow-velocity zones. *Nature*, *551*(7681), 494–497. https://doi.org/10.1038/nature24461

Liu, T., & Jing, Z. (2024a). Hydrogen and silicon are the preferred light elements in Earth's core. *Communications Earth & Environment*, *5*(1), 282. https://doi.org/10.1038/s43247-024-01450-3

Liu, T., & Jing, Z. (2024b). Thermoelastic properties of B2-type FeSi under deep Earth conditions: Implications for the compositions of the ultralow-velocity zones and the inner core. *Journal of Geophysical Research: Solid Earth*, *129*(4), e2023JB028539. https://doi.org/10.1029/2023jb028539

Mao, W. L., Mao, H.-K., Sturhahn, W., Zhao, J., Prakapenka, V. B., Meng, Y., et al. (2006). Iron-rich post-perovskite and the origin of ultralow-velocity zones. *Science*, *312*(5773), 564–565. https://doi.org/10.1126/science.1123442

Meeker, D. (2010). Finite element method magnetics. *FEMM*, *4*(32), 162.

Mergner, V., Kupenko, I., Spiekermann, G., Petitgirard, S., Libon, L., Chariton, S., et al. (2021). Sound velocities in FeSi at lower mantle conditions and the origin of ultralow-velocity zones. *Geophysical Research Letters*, *48*(14), e2020GL092257. https://doi.org/10.1029/2020gl092257

Mermin, N. D. (1965). Thermal properties of the inhomogeneous electron gas. *Physical Review*, *137*(5A), A1441–A1443. https://doi.org/10.1103/physrev.137.a1441

Pachhai, S., Li, M., Thorne, M. S., Dettmer, J., & Tkalčić, H. (2022). Internal structure of ultralow-velocity zones consistent with origin from a basal magma ocean. *Nature Geoscience*, *15*(1), 79–84. https://doi.org/10.1038/s41561-021-00871-5

Perdew, J. P., Burke, K., & Ernzerhof, M. (1996). Generalized gradient approximation made simple. *Physical Review Letters*, *77*(18), 3865–3868. https://doi.org/10.1103/physrevlett.77.3865

Pozzo, M., Davies, C., Gubbins, D., & Alfe, D. (2012). Thermal and electrical conductivity of iron at Earth's core conditions. *Nature*, *485*(7398), 355–358. https://doi.org/10.1038/nature11031

Reasoner, C., & Revenaugh, J. (2000). ScP constraints on ultralow-velocity zone density and gradient thickness beneath the Pacific. *Journal of Geophysical Research*, *105*(B12), 28173–28182. https://doi.org/10.1029/2000jb900331

Rost, S., Garnero, E. J., & Williams, Q. (2006). Fine-scale ultralow-velocity zone structure from high-frequency seismic array data. *Journal of Geophysical Research*, *111*(B9), B09310. https://doi.org/10.1029/2005jb004088

Sun, T., Brodholt, J. P., Li, Y., & Vočadlo, L. (2018). Melting properties from ab initio free energy calculations: Iron at the Earth's inner-core boundary. *Physical Review B*, *98*(22), 224301. https://doi.org/10.1103/physrevb.98.224301

Terada, Y., Ohkubo, K., Mohri, T., & Suzuki, T. (2002). Thermal conductivity of intermetallic compounds with metallic bonding. *Materials Transactions*, *43*(12), 3167–3176. https://doi.org/10.2320/matertrans.43.3167

Wang, D., Wu, Z., & Deng, X. (2023). Thermal conductivity of Fe-bearing bridgmanite and post-perovskite: Implications for the heat flux from the core. *Earth and Planetary Science Letters*, *621*, 118368. https://doi.org/10.1016/j.epsl.2023.118368

Wicks, J. K., Jackson, J. M., Sturhahn, W., & Zhang, D. (2017). Sound velocity and density of magnesiowüstites: Implications for ultralow-velocity zone topography. *Geophysical Research Letters*, *44*(5), 2148–2158. https://doi.org/10.1002/2016gl071225

Williams, Q., & Garnero, E. J. (1996). Seismic evidence for partial melt at the base of Earth's mantle. *Science*, *273*(5281), 1528–1530. https://doi.org/10.1126/science.273.5281.1528

Williams, Q., Revenaugh, J., & Garnero, E. (1998). A correlation between ultra-low basal velocities in the mantle and hot spots. *Science*, *281*(5376), 546–549. https://doi.org/10.1126/science.281.5376.546

Xu, J., Zhang, P., Haule, K., Minar, J., Wimmer, S., Ebert, H., & Cohen, R. E. (2018). Thermal conductivity and electrical resistivity of solid iron at Earth's core conditions from first principles. *Physical Review Letters*, *121*(9), 096601. https://doi.org/10.1103/physrevlett.121.096601

Yu, S., & Garnero, E. J. (2018). Ultralow velocity zone locations: A global assessment. *Geochemistry, Geophysics, Geosystems*, *19*(2), 396–414. https://doi.org/10.1002/2017gc007281

Zhang, Y., Hou, M., Liu, G., Zhang, C., Prakapenka, V. B., Greenberg, E., et al. (2020). Reconciliation of experiments and theory on transport properties of iron and the geodynamo. *Physical Review Letters*, *125*(7), 078501. https://doi.org/10.1103/physrevlett.125.078501

Zhang, Y., Luo, K., Hou, M., Driscoll, P., Salke, N. P., Minar, J., et al. (2022). Thermal conductivity of Fe-Si alloys and thermal stratification in Earth's core. *Proceedings of the National Academy of Sciences of the United States of America*, *119*(1), e2119001119. https://doi.org/10.1073/pnas.2119001119

Zhao, K., Jiang, G., & Wang, L. (2011). Electronic and thermodynamic properties of B2-FeSi from first principles. *Physica B: Condensed Matter*, *406*(3), 363–367. https://doi.org/10.1016/j.physb.2010.10.065